Journal of Magnetism and Magnetic Materials 408 (2016) 206–212

Contents lists available at ScienceDirect

Journal of Magnetism and Magnetic Materials

journal homepage: www.elsevier.com/locate/jmmm

Size dependent magnetic and magneto-optical properties of $Ni_{0.2}Zn_{0.8}Fe_2O_4$ nanoparticles

Oksana A. Li [a,b,*], Chun-Rong Lin [a,**], Hung-Yi Chen [a], Hua-Shu Hsu [a], Kun-Yauh Shih [c], Irina S. Edelman [d], Kai-Wun Wu [a], Yaw-Teng Tseng [a], Sergey G. Ovchinnikov [b,d], Jiann-Shing Lee [a]

[a] Department of Applied Physics, National Pingtung University, Pingtung 90003, Taiwan
[b] Siberian Federal University, Krasnoyarsk 660041, Russia
[c] Department of Applied Chemistry, National Pingtung University, Pingtung 90003, Taiwan
[d] L.V. Kirensky Institute of Physics, SB RAS, Krasnoyarsk 660036, Russia

ARTICLE INFO

Article history:
Received 7 August 2015
Received in revised form
9 February 2016
Accepted 19 February 2016
Available online 21 February 2016

Keywords:
Nickel zinc ferrite
Nanoparticles
Magnetic properties
MCD

ABSTRACT

$Ni_{0.2}Zn_{0.8}Fe_2O_4$ spinel nanoparticles have been synthesized by combustion method. Average particles size varies from 15.5 to 50.0 nm depending on annealing temperature. Correlations between particles size and magnetic and magneto-optical properties are investigated. Magnetization dependences on temperature and external magnetic field correspond to the sum of paramagnetic and superparamagnetic response. Critical size of single-domain transition is found to be 15.9 nm. Magnetic circular dichroism (MCD) studies of nickel zinc spinel are presented here for the first time. The features in magnetic circular dichroism spectrum are assigned to the one-ion d–d transitions in Fe^{3+} and Ni^{2+} ions, as well to the intersublattice and intervalence charge transfer transitions. The MCD spectrum rearrangement was revealed with the change of the nanoparticles size.

1. Introduction

High resistivity, low dielectric loss, excellent chemical stability and mechanical hardness make nanosized ferrites attractive for microwave and high frequency applications and as ferro-fluids and biomedical materials [1–7]. Nickel zinc ferrites find applications as the electronic sensor materials, for example, sensor for humidity measurement [8] and ethanol detection [9]; polymer composites with ferrite filler are perspective materials for absorbing electromagnetic waves at low radio frequency [10].

Spinels have formula $M1^{2+}M2_2^{3+}O_4^{2-}$ and crystallize in the cubic crystal system, with the oxygen anions arranged in a face centered-cubic lattice, and the cations M1 and M2 occupying 8 of 64 tetrahedral (A) and 16 of 64 octahedral (B) sites in the lattice [11]. In spinel oxides, A–O–A, B–O–B and A–O–B superexchange coupling through an oxygen anion exists. Among these interactions the A–O–B interaction is the strongest, the B–O–B is weaker and A–O–A is the weakest [12–14]. The spins of magnetic ions at the same sites are parallel and the spins of ions at different sites are oppositely oriented. Hence two oppositely magnetized sublattices occur. The resultant magnetization appears as difference between magnetizations of these two sublattices [11,12]. Magnetic properties are governed both by chemical composition and by cation distribution among tetrahedral and octahedral sites.

Bulk zinc ferrite $ZnFe_2O_4$ has a normal spinel structure, in which the Zn^{2+} cations occupy *A* sites and Fe^{3+} cations occupy *B* sites. Weak negative B–O–B interactions cause antiferromagnetic ordering of magnetic moments at low temperatures [15]. So zinc ferrite exhibits antiferromagnetic order with Neel temperature of about 10 K and becomes paramagnetic above this temperature [16–20].

According to Lotgering [19], a small fraction of Fe^{3+} cations in $ZnFe_2O_4$ occupies the *A* sites and form clusters with 12 neighboring Fe^{3+} ions at the *B* sites through a coupling by strong A–O–B interaction. Some authors found that the amount of Fe^{3+} in the *A* site and Zn^{2+} in the *B* site increases with the particle size decrease [21–23]. Ligenza reported that in polycrystalline $ZnFe_2O_4$ obtained by standard ceramic technique 4% of the Fe^{3+} ions located in the *A* sites [22]. Kamiyama et al. [23] reported that in nanocrystalline $ZnFe_2O_4$ prepared by coprecipitation method 10.2% of Fe^{3+} and 94.3% of Zn^{2+} cations were on the *A* sites for the fine particles

* Corresponding author at: National Pingtung University, Pingtung 90003, Taiwan.
** Corresponding author.
E-mail addresses: log85@mail.ru (O.A. Li), crlin@mail.nptu.edu.tw, crlinspin@gmail.com (C.-R. Lin).

http://dx.doi.org/10.1016/j.jmmm.2016.02.062
0304-8853/

with diameter of 96 nm and 13.3% of Fe^{3+} and 92.4% of Zn^{2+} cations were on the *A* sites for the fine particles with diameter of 29 nm.

Nickel ferrite, $NiFe_2O_4$, has an inverse spinel structure, in which Fe^{3+} ions occupy both *A* and *B* sites, and Ni^{2+} ions occupy B sites. Nickel ferrite is the ferrimagnetic material with the Curie temperature of about 865 K [24] and saturation magnetization of 56 emu/g at 0 K and 50 emu/g at 293 K [25]. $NiFe_2O_4$ nanoparticles were synthesized in Ref. [26] using the microwave heating of the bulk $NiFe_2O_4$ samples at various temperatures. The nanoparticles synthesized occurred to be of the inverse spinel cubic structure with good crystallinity and with the saturation magnetization of 31–45 emu/g at room temperature in dependence on the crystallite size (9, 10, and 12 nm). All samples demonstrated superparamagnetic behavior. Therefore, transition from bulk to nanosized state of $NiFe_2O_4$ does not change the substance structure and magnetic phase but leads to a decrease of the saturation magnetization

Mixed Ni–Zn ferrites are the research target of many authors because of their use as various inductance components, such as magnetic cores of filters, transformers, deflection, and so on, as well as the potential applications in magnetic liquid absorbing materials [27–29].

In nickel zinc ferrites nickel cations normally occupy an octahedral sites, whereas the zinc cations occupy tetrahedral sites [11,30,31]. However, some authors notice redistribution of cations in nanosized Ni–Zn ferrites. Morrison et al. [30] discovered that 39% of zinc cations and 95% of nickel cations were in octahedral sites in $Ni_{0.20}Zn_{0.44}Fe_{2.36}O_4$ nanoparticles with diameter $d=7$ nm obtained by a reverse micelle process. Kazin et al. [9] indicated that 75% of zinc cations, 60% of Fe^{3+} cations, and all nickel cations were in octahedral sites in $Ni_{0.2}Zn_{0.8}Fe_2O_4$ nanoparticles with $d=10$ nm synthesized using spray pyrolysis. Methods of the nanoparticles synthesis can play the decisive role in cation distribution and, hence, in their magnetic properties formation and, consequently, in their possible applications. In this paper, we report the synthesis of $Ni_{0.2}Zn_{0.8}Fe_2O_4$ nanoparticles of different size by combustion method and results of the study of their magnetic and magneto-optical properties in dependence on particles size.

2. Experimental details

Analytical grade nitrates $Ni(NO_3)_2\cdot 6H_2O$, $Zn(NO_3)_2\cdot 6H_2O$, $Fe(NO_3)_3\cdot 9H_2O$, citric acid monohydrate ($C_6H_8O_7\cdot H_2O$), and glycine (NH_2CH_2COOH) were dissolved in distilled water and mixed in an appropriate ratio to form a solution. The solution was concentrated by heating it in a cylindrical Pyrex dish until excess free water evaporated and spontaneous ignition occurred. The combustion was finished within a few seconds giving rise to a green black residue filling container. Then, this precursor residue was heated in air at different temperatures ranged from 200 to 1100 °C for one hour to obtain powders with different particles sizes.

The crystal structure and phase purity of all the samples were characterized by the X-ray powder diffraction (XRD). XRD measurements were performed using Cu Kα radiation, obtained with a rotating-anode X-ray generator operating at 50 kV and 200 mA and a graphite (002) monochromator. XRD patterns were measured at room temperature by step scanning in the angle 2θ ranged from 10º to 70º with an increment of 0.02º. The particle shape and size of samples were observed by the transmission electron microscope (TEM) Philips/FEI Tecnai G2 F20. A vibrating sample magnetometer (VSM) was used to measure magnetic properties. Field dependences of magnetization were measured at temperature 78 K under a magnetic field varied from −11 to 11 kOe. Temperature dependences of magnetization were measured at temperatures from 77 to 420 K in an applied field of 50 Oe. Magnetic circular dichroism (MCD) spectra were measured by J815 CD-spectrometer under a magnetic field of 7800 Oe at room temperature. Special samples were prepared for these measurements consisting of nanoparticles embedded into transparent non-magnetic matrices.

3. Results and discussion

3.1. Morphology and composition of $Ni_{0.2}Zn_{0.8}Fe_2O_4$ nanoparticles

TEM images of the $Ni_{0.2}Zn_{0.8}Fe_2O_4$ precursor are shown in Fig. 1. Fig. 1(a) shows that particles are uniform in size and tend to agglomerate. Fig. 1(b) shows high resolution TEM (HRTEM) image of the nanoparticle, one can see a lattice fringe spacing of 0.48 nm, which represents the (111) planes of the spinel ferrite. The agglomeration increases with annealing, which provides obtaining of series of nanoparticles with growing average size as the annealing temperature increase.

The XRD patterns of all annealed samples are shown in Fig. 2. XRD spectra reveal that all the samples are single phase ferrites with the spinel structure. The increase of the annealing temperature leads to the sharpness of all peaks, that is, to the increase of

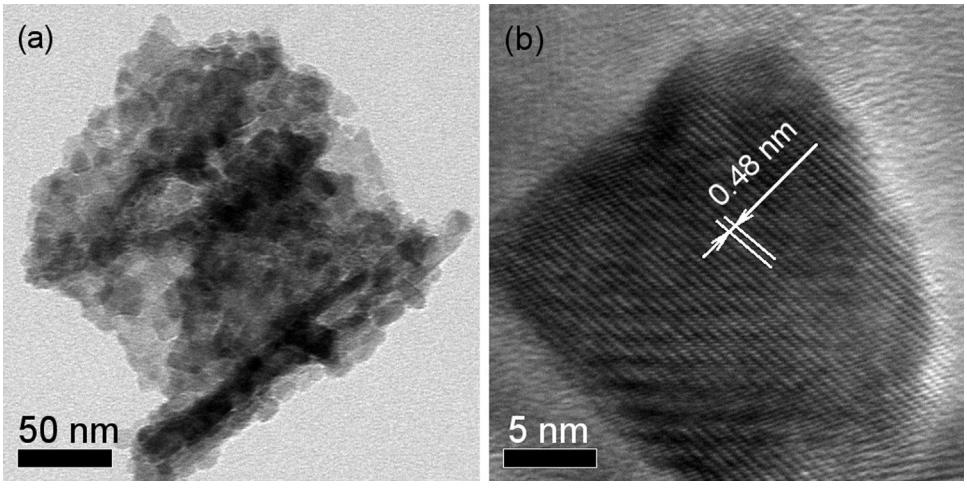

Fig. 1. The TEM image of the $Ni_{0.2}Zn_{0.8}Fe_2O_4$ nanoparticles (a) and HRTEM image (b) of the separate particle with atomic planes. Inter planes distance is 0.48 nm that corresponds to the (111) plane of $Ni_{0.2}Zn_{0.8}Fe_2O_4$.

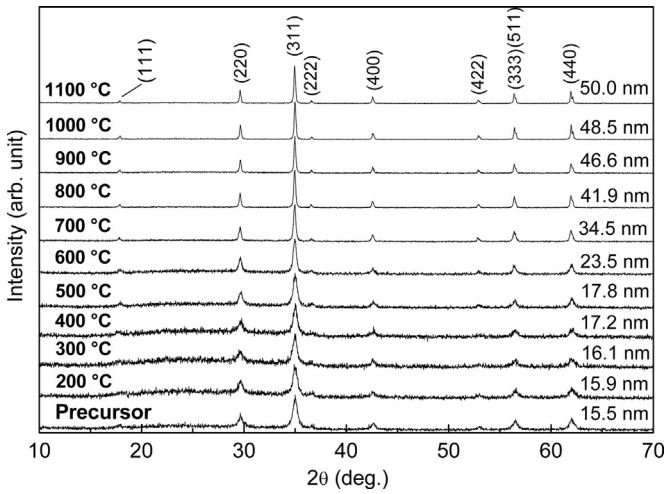

Fig. 2. X-ray diffraction patterns of $Ni_{0.2}Zn_{0.8}Fe_2O_4$ powders. The reflection indexes correspond to spinel phase. Average particles sizes estimated by Scherrer's formula are shown.

the crystalline size of $Ni_{0.2}Zn_{0.8}Fe_2O_4$ powders. The average crystallite size d was estimated from the most intensive (311) peak using Scherrer's formula $d=K\lambda/\Delta(2\theta)\cdot\cos\theta$. Here d is the average size of crystallites, K is the dimensionless shape factor assumed to be 0.94, $\lambda=0.15406$ nm is the wavelength for the Cu Kα radiation source, θ is the Bragg angle and $\Delta(2\theta)$ is the full width of the diffraction peak at half maximum located at 2θ. The average particles size varied from 15.9 to 50.0 nm with annealing temperature increased from 200 to 1100 °C. Thus, we have, indeed, the series of the nanoparticle powder samples fabricated with the same process and characterized by the same crystal structure but differing from each other by size.

3.2. Magnetic properties of $Ni_{0.2}Zn_{0.8}Fe_2O_4$ nanoparticles

Hysteresis loops at 78 K for the $Ni_{0.2}Zn_{0.8}Fe_2O_4$ samples obtained at different annealing temperatures are shown in Fig. 3(d–i). Magnetization does not reach saturation even in the highest field of 11 kOe. The shape of hysteresis loops indicates the presence of particles being in ferrimagnetic and apparently in superparamagnetic states. It is in agreement with result of [32] where Albuquerque et al. observed superparamagnetism at room temperature in nickel zinc ferrite with diameter of particles up to 90 nm.

Dependence of magnetization M on external field H was fitted using following equation:

$$M(H) = a_0 - a_1H^{-2} + a_2L(H/a_3) \quad (1)$$

here $L(x)=cth(x)-1/x$ is the Langevin function.

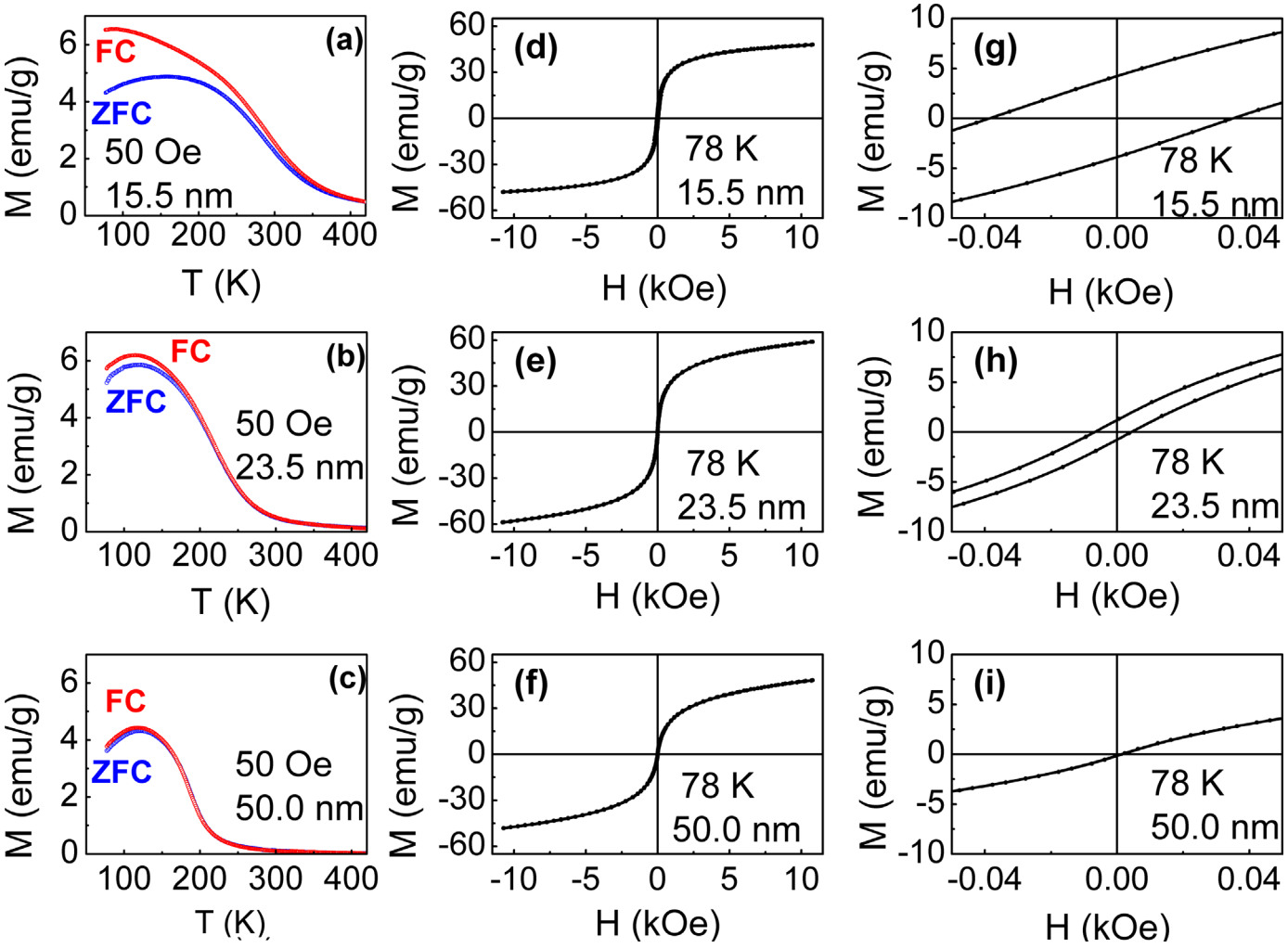

Fig. 3. Magnetization dependences on temperature (a–c) and on the applied magnetic field (d–f) for the $Ni_{0.2}Zn_{0.8}Fe_2O_4$ nanoparticles with various average diameters. Fig. (g–i) shows the zoomed view of hysteresis plots.

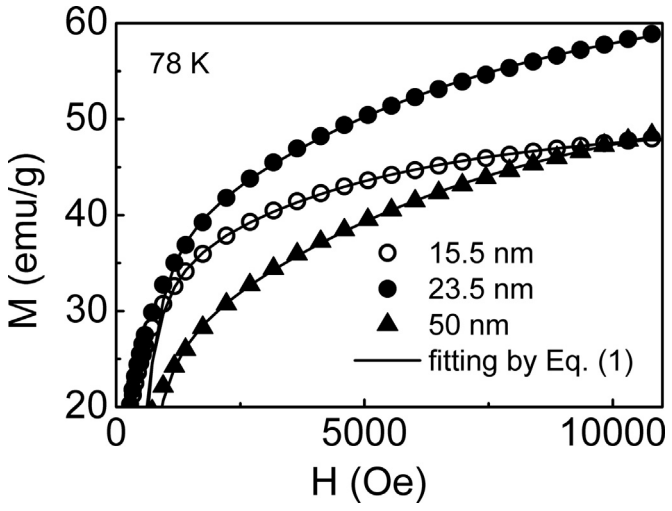

Fig. 4. Approach of magnetization to saturation.

Table 1
Values of magnetic parameters of $Ni_{0.2}Zn_{0.8}Fe_2O_4$ powders.

Particles size d, nm	$a_0=M_f$, emu/g	$a_2=M_{sp}$, emu/g	M_{tot}, emu/g	aH_{fa}, Oe
15.5	33.7	18.2	51.9	413
23.5	36.6	32.0	68.6	455
50.0	25.2	33.6	58.8	520

The first two terms in this expression correspond to Akulov law [33] that describes the magnetization curve in the region of approach to saturation for ferromagnetic phase. Here $a_0=M_f\nu_f$; $a_1=M_f\nu_f aH_{fa}^2$, M_f is the average magnetization of the ferromagnetic particles, ν_f is the volume fraction of this component, aH_{fa} is root-mean-square fluctuation of local magnetic anisotropy field H_{fa} [34]. The third term in (1) describes the magnetization dependence on applied field for superparamagnetic particles in accordance with the Langevin law, where $a_2=M_{sp}\nu_{sp}$; $a_3=k_BT/M_{sp}V_{sp}$. Here M_{sp} is the average magnetization of the superparamagnetic phase, ν_{sp} is the volume fraction of this component, and V_{sp} is the average volume of a superparamagnetic particle [35]. Fig. 4 shows a good fitting of magnetization dependence curve by function (1) in applied fields higher than 1 kOe. The values of fitting parameters allow one to determine the values of average root-mean-square fluctuation of local magnetic anisotropy field in ferromagnetic phase $aH_{fa}=(a_1/a_0)^{1/2}$, the value of magnetization per gram $M_{tot}=M_{sp}\nu_{sp}+M_f\nu_f=a_2+a_0$. The determined values of physical properties found are given in Table 1.

Coercive force (H_c) increases with average diameter decreasing until it reaches its maximum value at $d=15.9$ nm, corresponding to annealing temperature 200 °C, then it decreases (Fig. 5). This critical diameter corresponds to a transition from multi-domain to a single-domain state. Critical single-domain size is 15.9 nm and is lower than 28 nm obtained by Modak et al [36] for $Ni_{0.4}Zn_{0.4}Cu_{0.2}Fe_2O_4$ and by Caizer et al. [37] for $Ni_{0.35}Zn_{0.65}Fe_2O_4$. Saturation magnetization is close to that of $Ni_{0.35}Zn_{0.65}Fe_2O_4$ nanoparticles with $d=46.3$ nm $M_S=58.3$ emu/g [37] and of $ZnFe_2O_4$ nanoparticles with $d=52$ nm $M_S=60$ emu/g [38].

The temperature dependences of magnetization were recorded for zero-field-cooled (ZFC) and field-cooled (FC) modes in an applied field of 50 Oe. The ZFC and FC curves of samples without annealing and of samples annealed at 200 and 300 °C with diameters of 15.5, 15.9 and 16.1 nm, respectively, are split in the whole range of temperatures up to 420 K. The ZFC and FC curves of samples annealed at 400, 500 and 300 °C with diameters of 17.2, 17.8 and 23.5 nm, respectively, are split at temperatures below

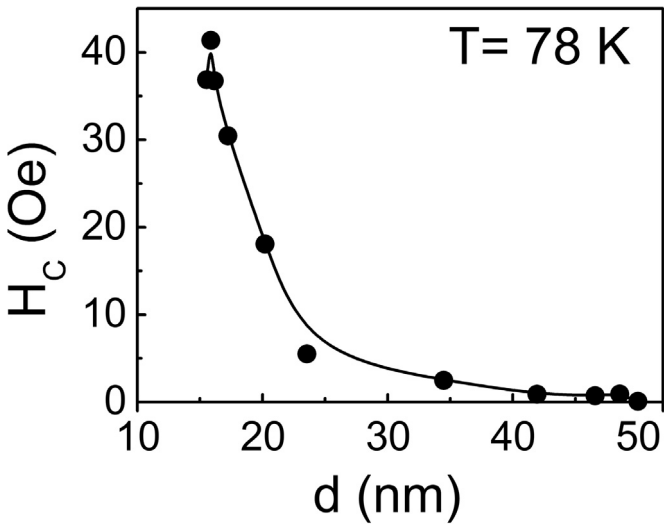

Fig. 5. Coercive force H_c dependence on average diameter of $Ni_{0.2}Zn_{0.8}Fe_2O_4$ nanoparticles.

330–400 K, it is irreversibility temperature at which the relaxation time of the largest particles becomes comparable to measuring time. The ZFC and FC curves of samples annealed at temperatures from 800 to 1100 °C i.e. with diameters from 41.9 to 50 nm slightly spilt below ~200 K.

The maximum in the ZFC curves corresponds to a mean blocking temperature T_B. Above this temperature, particles are in a superparamagnetic state, whereas below T_B, magnetic anisotropy disables thermal fluctuations of magnetic moments and particles are in a ferrimagnetic state. The width of the peak for smaller particles is larger indicating the wider distribution of blocking temperatures because of the wider distribution of particle size. Dependence of blocking temperature on particles size is shown in Fig. 6.

The Curie temperatures (T_c) of $Ni_{0.2}Zn_{0.8}Fe_2O_4$ powders were estimated from the position of inflection point in $M(T)$ curve, i.e. the position of the minimum of $M(T)$ derivative with respect to temperature. Curie temperature dependence on particles size is shown in Fig. 7.

Dependence of magnetic properties on particles size can be due to change in distribution of cations when the grain size decreases to the nano-size. A part of Zn^{2+} may enter into B-site and Fe^{3+} and Ni^{2+} enter into A-site simultaneously. As a result, a Curie temperature increases, which attributes to the enhancement of the A–B interaction.

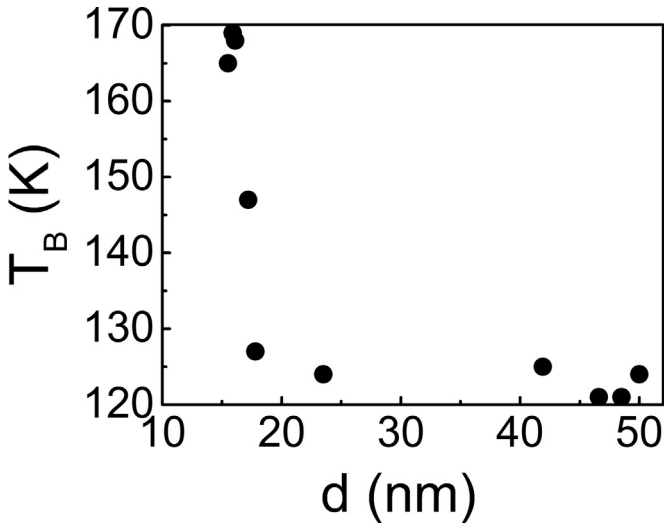

Fig. 6. Dependence of blocking temperature T_B on particles size d.

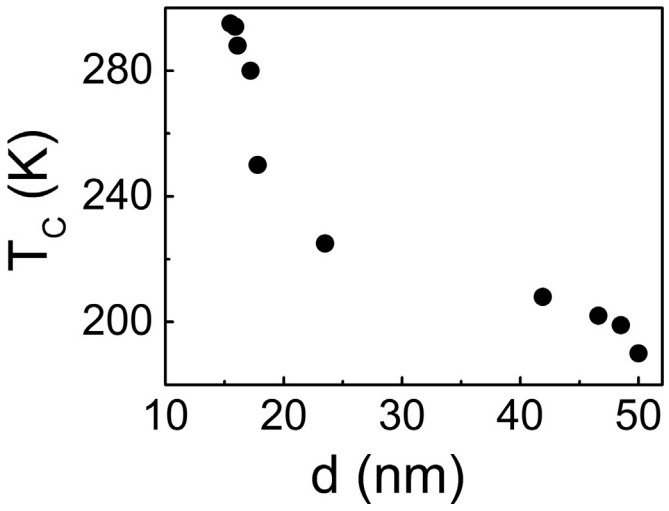

Fig. 7. Curie temperature T_c dependence on average diameter d of $Ni_{0.2}Zn_{0.8}Fe_2O_4$ nanoparticles.

3.3. *Magneto-optical properties of $Ni_{0.2}Zn_{0.8}Fe_2O_4$ nanoparticles*

The results of the room temperature MCD measurements are shown in Fig. 8. A wide maximum at 320–370 nm (3.35–3.87 eV) consisting of several overlapping peaks and more sharp maximum at ~465 nm with satellite at ~530 nm (2.66 and 2.34 eV, correspondingly) are observed in all samples. The higher is the annealing temperature and thus the higher is the average diameter of the particles, the lower intensity of the MCD maxima is observed. It is in agreement with the magnetization measurements data, according to which magnetization reduces with the particles diameter increase. Though the difference between the magnetization values of smallest and largest particles is of about 30 percentages at low temperatures, it increases several times at room temperature because of the Curie temperature lowering with the particles size increase (see, Fig. 3(a, b, and c)). As the MCD measurements were carried out at room temperature, its magnitude dependence on the particles size may be distorted by the dependence on temperature. Therefore, for an adequate comparison between samples it is possible to use only the positions of the MCD spectral features.

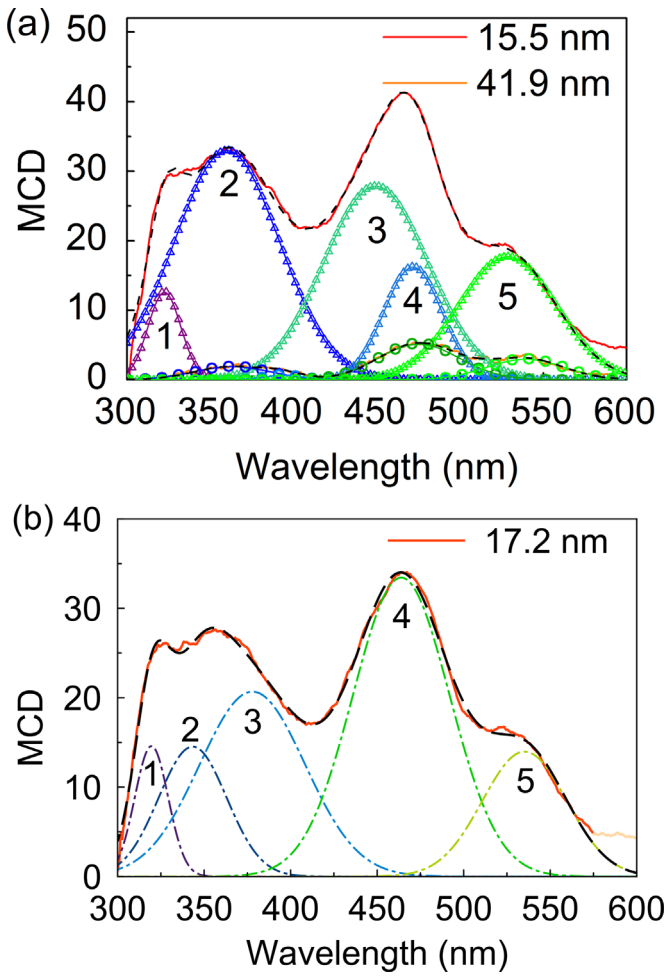

Fig. 8. MCD spectra of $Ni_{0.2}Zn_{0.8}Fe_2O_4$ nanoparticles with (a) $d=15.5$ nm, $d=41.9$ nm and (b) $d=17.2$ nm at magnetic field of 7800 Oe and room temperature. Gauss components (triangles, circles and dash dotted lines for particles with $d=15.5$, 41.9 and 17.2 nm, respectively) and approximation of experimental data by sum of Gaussians (long dash lines) are shown.

To extract the spectral parameters we have decomposed the MCD spectra to Gauss components. The results of decomposition are given in Table 2. The maxima positions and intensities depend on an average particles size. At that, the main changes in the maximum positions occur when the particles size changes from 15.5 to 17.2 nm (compare Fig. 8(a) and (b)), that is at the transition from mono- to multi-domain particles. In the lower wavelength region, two peaks (2 and 3 in Fig. 8(b)) appeared for the larger particle dimensions instead of one (2 in Fig. 8(a)) for the lower particle dimensions. At the middle wavelength region, vice versa, one intense peak (4 in Fig. 8) appears at the particle dimensions increase instead of two less intense peaks (3 and 4 in Fig. 8(a)) for smaller particles. Only peaks 1 and 5 are observed at the same wavelengths for all samples.

Magneto-optical effects in iron oxides are determined by electron transitions of different nature. The main are: (i) charge transfer transitions between paramagnetic ions and their ligands; (ii) one-ion d–d transitions between ground and excited states of an ion splitted by the crystal field (CF); (iii) transitions between ions in different sub-lattices–inter-sub-lattice charge transfer transitions (ISCT); (iv) transitions between ions of different valence states–inter-valence charge transfer transitions (IVCT). The first type of transitions occurs, usually, at high energies in the ultra violet region.

The d–d transitions in Fe^{3+} ion of $3d^5$ electron configuration from the ground $^6A_1(^6S)$ state to the excited states are both spin and parity forbidden inside the isolated atom. However, in crystal these transitions may occur with a definite transition probability due to the so-called pair excitations resulting from the simultaneous excitation of two neighboring cations that are magnetically coupled [39–44]. For example, the pair transitions ($^6A_1+{}^6A_1\rightarrow{}^4T_1+{}^4T_1$) [45,46] involving the simultaneous excitation of magnetically coupled two neighboring Fe^{3+} ions from the oppositely magnetized sub-lattices becomes spin allowed and have higher probability than the spin-forbidden transition [44]. Hashimoto et al. [44] considered this type of transitions to be responsible for the absorption spectrum peculiarities at 2.2–2.4 eV (515–565 nm) in the γ-Fe_2O_3 thin films with spinel structure where Fe^{3+} ions occupy octahedral and tetrahedral positions. At the same time, authors of Ref. [47] assigned peak at 2.8 eV (440 nm) observed in the MCD spectrum of γ-Fe_2O_3 nanoparticles to the same pair excitation process ($^6A_1+{}^6A_1\rightarrow{}^4T_1+{}^4T_1$). Authors of Ref. [48] ascribed two maxima at 2.6 eV and 2.3 eV (480 and 540 nm, correspondingly) observed in the MCD spectrum of the γ-Fe_2O_3 thin films to the $^6A_1(^6S)\rightarrow{}^4A_1$, $^4E(^4G)$ CF transitions of Fe^{3+} in tetrahedral and octahedral sites, respectively. These authors observed also a peak at 3.02 eV (410 nm) and ascribed it to the charge-transfer transitions of the $t_{2u}(\pi)\rightarrow t_{2g}$, $t_{1u}(\pi)\rightarrow t_{2g}$ and $t_{1u}(\sigma)\rightarrow t_{2g}$ types or to $^6A_1(^6S)\rightarrow{}^4T_2(^4D)$ CF transition. Authors of

Table 2
Wavelengths λ and intensities I of the Gaussian peaks in the MCD spectra of $Ni_{0.2}Zn_{0.8}Fe_2O_4$ nanoparticles with different average diameters

Peak no.	d=15.5 nm		d =17.2 nm		d =17.8 nm		d =23.5 nm		d =41.9 nm	
	λ, nm	I, arb. units	λ, nm	I, arb. units	λ, nm	I, arb. units	λ, nm	I, arb. units	λ, nm	I, arb. units
1	322	12.7	320	14.6	319	8.2	319	7.1	–	–
2	360	33.0	343	14.5	339	5.5	336	6.4	363	1.9
3	449	27.9	378	20.7	368	14.0	372	10.1	394	0.7
4	472	16.3	464	33.4	463	19.7	462	15.3	475	5.3
5	529	17.7	535	14.0	538	7.2	536	5.4	539	3.0

[49] observed intense maximum at 450 nm (2.75 eV) and less intense maximum of the same sign at 660 nm (1.88 eV) in the MCD spectrum of the $Mn_xFe_{3-x}O_4$ films and referred them to the CF electron transitions $^6A_{1g}\rightarrow{}^4E_g$, $^4A_{1g}$ and $^6A_{1g}\rightarrow{}^4T_{2g}$ in Fe^{3+} ions occupying octahedral positions.

There are no data on the magneto-optical spectra of nickel–zinc ferrites in the current literature. That is why we can rely on the investigations of the magneto-optical Kerr effect (MOKE) in $NiFe_2O_4$ carried out by several authors. Kim et al. measured MOKE spectra for the $NiFe_2O_4$ films with thicknesses of about 1 μm fabricated by sol–gel technique [50] and identified the spectra features at 2.2, 2.6, 3.1, 4.0, and 4.5 eV with definite electron transitions. Fontijn et al. [41,42] used the MOKE of the $NiFe_2O_4$ single crystal to calculate the off-diagonal components of the dielectric tensor, ε_{xy}, and have obtained the ε_{xy} spectrum features at 2.57, 2.86, and 4.03 eV. Himcinschi et al. [51] used the same approach for the $NiFe_2O_4$ epitaxial thin films grown with pulsed-laser deposition. The energies of the ε_{xy} features were in this case as follows: 1.89, 2.52, 3.15, 4.15, and 4.62 eV. Discrepancies between the MOKE spectral feature positions observed by different authors can be associated, particularly, with the different distribution of the paramagnetic ions between crystal sites in the specific samples. In spite of these differences three groups of authors gave the same identification of the resonant features. These are the next five transitions (from lower to higher energy): CF transition in Ni^{2+} ions $^3T_{1g}(^3F)\rightarrow{}^3A_{2g}(^3F)$; ISCT $(Fe^{3+})t_2\rightarrow[Fe^{3+}]t_{2g}$; IVCT $[Ni^{2+}]t_{2g}\rightarrow[Fe^{3+}]t_{2g}$; ISCT $(Fe^{3+})t_2\rightarrow[Fe^{3+}]e_g$; IVCT $[Ni^{2+}]t_{2g}\rightarrow[Fe^{3+}]t_2$. Here, the parentheses denote tetrahedral sites and the square brackets denote the octahedral sites in ferrite lattice.

Turn now to the MCD spectrum. The lower energy maxima observed near 2.3 and 2.6 eV (peaks 5 and 4, correspondingly, in Fig. 8(a)) coincide, according to their positions, with the MCD maxima of the γ-Fe_2O_3 thin films [48] and analogously can be referred to the on-ion CF transitions of Fe^{3+} in octahedral $^6A_{1g}(^6S)\rightarrow{}^4A_{1g}$, $^4E_g(^4G)$ and tetrahedral $^6A_1(^6S)\rightarrow{}^4A_1$, $^4E(^4G)$ sites. The CF transition energy should depend insignificantly on the particles dimension that is fulfilled for the peak 5. Peak 4 is located in an area where it partially overlaps with stronger peak 3 (Fig. 8) If one of these peaks (or both peaks) intensity increases with the particles size increase, two peaks can convert to one. Peak 3 can be due to IVCT $[Ni^{2+}]t_{2g}\rightarrow[Fe^{3+}]t_{2g}$. For samples with smaller particles, this peak loses intensity as a part of the Fe^{3+} ions shifts to tetrahedral positions. In samples with larger particles, the number of Fe^{3+} ions in octahedral sites increases, intensity of transition associated with these ions increases and two peaks seen separately in Fig. 8(a) for the smaller particles merge into one intense peak for the larger particles (Fig. 8(b)).

Similar picture is observed in the region of 359–400 nm with opposite behavior: intense peak for the smaller particles converts to two peaks for the larger particles. Such a behavior can be due to the charge transfer between tetrahedral and octahedral Fe^{3+} ions ISCT $(Fe^{3+})t_2\rightarrow[Fe^{3+}]e_g$ and ISCT $(Fe^{3+})t_2\rightarrow[Fe^{3+}]t_{2g}$. With an increase of the tetrahedral ions in the case of smaller particles, these transitions intensity decreases and two peaks merge into one. Peak 1 is reasonable to associate with the IVCT: $[Ni^{2+}]t_{2g}\rightarrow[Fe^{3+}]t_2$. Its intensity depends also on the Fe^{3+} number in octahedral positions and, consequently, it should decrease with the particles size. Indeed, these peak intensity decreases at the nanoparticle dimension decrease from 17.2 nm to 15.5 nm in spite of the magnetization increase. It is possible to make such a comparison for these two sizes, as far as for the larger nanoparticles very strong room temperature magnetization decrease with the particles size increase is superior to all other effects.

The MCD peaks identification presented here do not contradict, in principal, the results of Refs. [41,42,50,51]. If it is valid, the MCD spectrum rearrangement with the particles size decrease could mean that the larger part of the Fe^{3+} ions removes to the tetrahedral positions in the smallest nanoparticles. To make conclusions that are more definite, it is necessary to investigate the temperature MCD dependences for all particles size in comparison with the magnetization temperature dependences at the same values of an external magnetic field that will allow separating of the MCD dependences on temperature and on the particles size. This work is in progress now.

4. Conclusions

$Ni_{0.2}Zn_{0.8}Fe_2O_4$ spinel nanoparticles were synthesized by facile combustion method with subsequent annealing. Sizes of particles are varied by annealing at different temperatures. X-ray diffraction data indicate single-phase spinel. Magnetic measurements show sum of superparamagnetic and ferromagnetic response. Critical size of single-domain transition found from maximum of coercive force dependence on particles size was estimated to be 15.9 nm.

MCD measurements of nickel zinc spinel are presented here for the first time. To extract the spectral parameters from the MCD data, we have decomposed the MCD spectra to several Gauss components and identified the component energies with the electron transitions of different nature in different parts of the investigated spectral region. The set of the proposed transitions includes CF transitions in Fe^{3+} and Ni^{2+} ions, the intersublattice and intervalence charge transfer transitions. The MCD spectrum rearrangement with the change of the nanoparticles size is associated with the change in the Fe^{3+} ions distribution between octahedral and tetrahedral crystal positions. Thus, MCD is shown to be a proper tool to study an influence of the particles size on the paramagnetic ions distribution among crystal sites.

Acknowledgments

This work is supported by the Ministry of Science and Technology of Taiwan (MOST 103-2811-M-153 -001 and MOST 102-2112-M-153 -002 -MY3), and by the Russian Foundation for Basic Researches, Grant no. 14-02-01211.

References

[1] A. Verma, D.C. Dube, Processing of nickel-zinc ferrites via the citrate precursor route for high-frequency applications, J. Am. Ceram. Soc. 88 (2005) 519–523, http://dx.doi.org/10.1111/j.1551-2916.2005.00098.x.

[2] M.N. Akhtar, N. Yahya, P. Bin Hussain, Structural and magnetic characterizations of nano structured $Ni_{0.8}Zn_{0.2}Fe_2O_4$ prepared by self combustion method, Int. J. Basic Appl. Sci. 09 (2009) 37–40, http://ijens.org/1928091-IJBAS.pdf.

[3] M. Kooti, A.N. Sedeh, Synthesis and characterization of $NiFe_2O_4$ magnetic nanoparticles by combustion method, J. Mater. Sci. Technol. 29 (2013) 34–38, http://dx.doi.org/10.1016/j.jmst.2012.11.016.

[4] E. Mazarío, P. Herrasti, M.P. Morales, N. Menéndez, Synthesis and characterization of $CoFe_2O_4$ ferrite nanoparticles obtained by an electrochemical method, Nanotechnology 23 (2012) 355708, http://dx.doi.org/10.1088/0957-4484/23/35/355708.

[5] A. Kumar, P. Kumar, G. Rana, M.S. Yadav, R.P. Pant, A study on structural and magnetic properties of $Ni_xZn_{1-x}Fe_2O_4$ ($0 \le x \le 0.6$) ferrite nanoparticles, Appl. Sci. Lett. 1 (2015) 33–36, http://dx.doi.org/10.17571/appslett.2015.01009.

[6] A. Kumar, A. Singh, M.S. Yadav, M. Arora, R.P. Pant, Finite size effect on Ni doped nanocrystalline $Ni_xZn_{1-x}Fe_2O_4$ ($0.1 \le x \le 0.5$), Thin Solid Films 519 (2010) 1056–1058, http://dx.doi.org/10.1016/j.tsf.2010.08.043.

[7] G.S. Shahane, A. Kumar, M. Arora, R.P. Pant, K. Lal, Synthesis and characterization of Ni–Zn ferrite nanoparticles, J. Magn. Magn. Mater. 322 (2010) 1015–1019, http://dx.doi.org/10.1016/j.jmmm.2009.12.006.

[8] S.N. Patil, B.P. Ladgaonkar, Synthesis and implementation of $NiZnFe_2O_4$ ferrites to design embedded system for humidity measurement, Int. J. Adv. Res. Electr. Electron. Instrum. Eng. 2 (2013) 3813–3821.

[9] A.P. Kazin, M.N. Rumyantseva, V.E. Prusakov, I.P. Suzdalev, A.M. Gaskov, Nanocrystalline ferrites $Ni_xZn_{1-x}Fe_2O_4$: Influence of cation distribution on acidic and gas sensing properties, J. Solid State Chem. 184 (2011) 2799–2805, http://dx.doi.org/10.1016/j.jssc.2011.08.029.

[10] T.F. Khoon, J. Hassan, N. Mokhtar, M. Hashim, N.A. Ibrahim, W.S. Yin, et al., Dielectric properties of $Ni_{0.2}Zn_{0.8}Fe_2O_4$-polypropylene composites, Am. J. Appl. Sci. 7 (2010) 1226–1230.

[11] J. Smit, H.P.J. Wijn, Ferrites, Phillips' Technical Library, Eindhoven, 1959.

[12] S. Dey, A. Roy, J. Ghose, R.N. Bhowmik, R. Ranganathan, Size dependent magnetic phase of nanocrystalline $Co_{0.2}Zn_{0.8}Fe_2O_4$, J. Appl. Phys. 90 (2001) 4138–4142, http://dx.doi.org/10.1063/1.1401798.

[13] J.L. Dormann, M. Nogues, Magnetic structures in substituted ferrites, J. Phys. Condens. Matter 2 (1990) 1223–1237, http://dx.doi.org/10.1088/0953-8984/2/5/014.

[14] C.E. Rodríguez Torres, F. Golmar, M. Ziese, P. Esquinazi, S.P. Heluani, Evidence of defect-induced ferromagnetism in $ZnFe_2O_4$ thin films, Phys. Rev. B. 84 (2011) 064404, http://dx.doi.org/10.1103/PhysRevB.84.064404.

[15] V.G. Vologin, V.D. Parkhomenko, S.F. Dubinin, Y.G. Chukalkin, B.N. Goshchitskii, S.K. Sidorov, et al., Exchange Fe^{3+}–Fe^{3+} interactions in ferrites with spinel structure, Phys. Status Solidi 33 (1976) K83–K86, http://dx.doi.org/10.1002/pssa.2210330244.

[16] C.N. Chinnasamy, A. Narayanasamy, N. Ponpandian, K. Chattopadhyay, H. Guérault, J.-M. Greneche, Magnetic properties of nanostructured ferrimagnetic zinc ferrite, J. Phys. Condens. Matter 12 (2000) 7795–7805.

[17] W. Schiessl, W. Potzel, H. Karzel, M. Steiner, G.M. Kalvius, A. Martin, et al., Magnetic properties of the $ZnFe_2O_4$ spinel, Phys. Rev. B. 53 (1996) 9143–9152, http://dx.doi.org/10.1103/PhysRevB.53.9143.

[18] F. Li, H. Wang, L. Wang, J. Wang, Magnetic properties of $ZnFe_2O_4$ nanoparticles produced by a low-temperature solid-state reaction method, J. Magn. Magn. Mater. 309 (2007) 295–299, http://dx.doi.org/10.1016/j.jmmm.2006.07.012.

[19] F.K. Lotgering, The influence of Fe^{3+} ions at tetrahedral sites on the magnetic properties of $ZnFe_2O_4$, J. Phys. Chem. Solids 27 (1966) 139–145.

[20] M. Hofmann, S.J. Campbell, H. Ehrhardt, R. Feyerherm, The magnetic behaviour of nanostructured zinc ferrite, J. Mater. Sci. 39 (2004) 5057–5065, http://dx.doi.org/10.1023/B:JMSC.0000039185.80910.59.

[21] M.R. Anantharaman, S. Jagatheesan, K.A. Malini, S. Sindhu, A. Narayanasamy, C. N. Chinnasamy, et al., On the magnetic properties of ultra-fine zinc ferrites, J. Magn. Magn. Mater. 189 (1998) 83–88, http://dx.doi.org/10.1016/S0304-8853(98)00171-1.

[22] S. Ligenza, A Study of the 6S5/2-Term Splitting of an Fe^{3+} Ion in Zinc Ferrite by Neutron Spectroscopy, Phys. Status Solidi 75 (1976) 315–326.

[23] T. Kamiyama, K. Haneda, T. Sato, S. Ikeda, H. Asano, Cation distribution in $ZnFe_2O_4$ fine particles studied by neutron powder diffraction, Solid State Commun. 81 (1992) 563–566, http://dx.doi.org/10.1016/0038-1098(92)90412-3.

[24] J.M.D. Coey, Magnetism and Magnetic Materials, Cambridge University Press, Cambridge, United Kingdom (2010) http://dx.doi.org/10.1017/CBO9780511845000.

[25] B.D. Cullity, C.D. Graham, Introduction to magnetic materials, second edition, Wiley-IEEE Press, Hoboken, New Jersey, 2009.

[26] W.S. Galvão, R.M. Freire, T.S. Ribeiro, I.F. Vasconcelos, L.S. Costa, V.N. Freire, et al., Cubic superparamagnetic nanoparticles of $NiFe_2O_4$ via fast microwave heating, J. Nanopart. Res. 16 (2014) 2803, http://dx.doi.org/10.1007/s11051-014-2803-6.

[27] F. Li, X. Liu, Q. Yang, J. Liu, D.G. Evans, X. Duan, Synthesis and characterization of $Ni_{1-x}Zn_xFe_2O_4$ spinel ferrites from tailored layered double hydroxide precursors, Mater. Res. Bull. 40 (2005) 1244–1255, http://dx.doi.org/10.1016/j.materresbull.2005.04.011.

[28] M. Mohapatra, B. Pandey, C. Upadhyay, S. Anand, R.P. Das, H.C. Verma, Effect of Ni doping on the properties of fine magnetite particles, J. Magn. Magn. Mater. 295 (2005) 44–50, http://dx.doi.org/10.1016/j.jmmm.2004.12.036.

[29] M. Sugimoto, The past, present, and future of ferrites, J. Am. Ceram. Soc. 82 (1999) 269–280, http://dx.doi.org/10.1111/j.1551-2916.1999.tb20058.x.

[30] S.A. Morrison, C.L. Cahill, E.E. Carpenter, S. Calvin, R. Swaminathan, M. E. McHenry, et al., Magnetic and structural properties of nickel zinc ferrite nanoparticles synthesized at room temperature, J. Appl. Phys. 95 (2004) 6392–6395, http://dx.doi.org/10.1063/1.1715132.

[31] Y.G. Chukalkin, V.R. Shtirts, Magnetic state of $ZnFe_2O_4$, Phys. Solid State (Fiz. Tverd. Tela) 30 (1988) 2919–2923.

[32] A.S. Albuquerque, J.D. Ardisson, W.A.A. Macedo, A study of nanocrystalline NiZn-ferrite–SiO_2 synthesized by sol–gel, J. Magn. Magn. Mater. 192 (1999) 277–280, http://dx.doi.org/10.1016/S0304-8853(98)00367-9.

[33] N.S. Akulov, Über den Verlauf der Magnetisierungskurve in starken Feldern, Zeitschrift Für Phys. Hadron. Nucl. 69 (1931) 822–831, http://dx.doi.org/10.1007/BF01339465.

[34] V.A. Ignatchenko, R.S. Iskhakov, G.V. Popov, Law of approach of the magnetization to saturation in amorphous ferromagnets, Sov. Phys. JETP 55 (1982) 878–886 ⟨⟨http://www.jetp.ac.ru/cgi-bin/dn/e_055_05_0878.pdf⟩⟩.

[35] R. Iskhakov, E. Denisova, L. Kuzovnikova, S. Komogortsev, A. Balaev, G. Bondarenko, Structure and magnetic features of nanostructured Co–Cu alloys synthesized by new modification of mechanochemical synthesis, J. Optoelectron. Adv. Mater. 10 (2008) 1043–1047.

[36] S. Modak, M. Ammar, F. Mazaleyrat, S. Das, P.K. Chakrabarti, XRD, HRTEM and magnetic properties of mixed spinel nanocrystalline Ni–Zn–Cu-ferrite, J. Alloy. Compd. 473 (2009) 15–19, http://dx.doi.org/10.1016/j.jallcom.2008.06.020.

[37] C. Caizer, M. Stefanescu, Magnetic characterization of nanocrystalline Ni–Zn ferrite powder prepared by the glyoxylate precursor method, J. Phys. D. Appl. Phys. 35 (2002) 3035–3040, http://dx.doi.org/10.1088/0022-3727/35/23/301.

[38] N.M. Deraz, A. Alarifi, Microstructure and magnetic studies of zinc ferrite nano-particles, Int. J. Electrochem. Sci. 7 (2012) 6501–6511.

[39] Y.P. He, Y.M. Miao, C.R. Li, S.Q. Wang, L. Cao, S.S. Xie, et al., Size and structure effect on optical transitions of iron oxide nanocrystals, Phys. Rev. B – Condens. Matter Mater. Phys. 71 (2005) 125411, http://dx.doi.org/10.1103/PhysRevB.71.125411.

[40] G.B. Scott, D.E. Lacklison, H.I. Ralph, J.L. Page, Magnetic circular dichroism and Faraday rotation spectra of $Y_3Fe_5O_{12}$, Phys. Rev. B 12 (1975) 2562–2571, http://dx.doi.org/10.1103/PhysRevB.12.2562.

[41] W.F.J. Fontijn, P.J. van der Zaag, R. Metselaar, On the origin of the magneto-optical effects in Li, Mg, Ni, and Co ferrite, J. Appl. Phys. 83 (1998) 6765–6767, http://dx.doi.org/10.1063/1.367992.

[42] W.F.J. Fontijn, P.J. van der Zaag, L.F. Feiner, R. Metselaar, M.A.C. Devillers, A consistent interpretation of the magneto-optical spectra of spinel type ferrites (invited), J. Appl. Phys. 85 (1999) 5100–5105, http://dx.doi.org/10.1063/1.369091.

[43] W.F.J. Fontijn, P.J. van der Zaag, M.A.C. Devillers, V.A.M. Brabers, R. Metselaar, Optical and magneto-optical polar Kerr spectra of Fe_3O_4 and Mg^{2+}- or Al^{3+}-substituted Fe_3O_4, Phys. Rev. B 56 (1997) 5432–5442, http://dx.doi.org/10.1103/PhysRevB.56.5432.

[44] T. Hashimoto, T. Yamada, T. Yoko, Third-order nonlinear optical properties of sol–gel derived α-Fe_2O_3, γ-Fe_2O_3, and Fe_3O_4 thin films, J. Appl. Phys. 80 (1996) 3184–3190, http://dx.doi.org/10.1063/1.363258.

[45] R.V. Morris, H.V. Lauer, C.A. Lawson, E.K. Gibson, G.A. Nace, C. Stewart, Spectral and other physicochemical properties of submicron powders of hematite (alpha-Fe_2O_3), maghemite (gamma-Fe_2O_3), magnetite (Fe_3O_4), goethite (alpha-FeOOH), and lepidocrocite (gamma-FeOOH), J. Geophys. Res. 90 (1985) 3126–3144, http://dx.doi.org/10.1029/JB090iB04p03126.

[46] H.J. Schugar, G.R. Rossman, J. Thibeault, H.B. Gray, Simultaneous pair electronic excitations in a binuclear iron(III) complex, Chem. Phys. Lett. 6 (1970) 26–28.

[47] E. Fantechi, G. Campo, D. Carta, A. Corrias, C. De Julián Fernández, D. Gatteschi, et al., Exploring the effect of Co doping in fine maghemite nanoparticles, J. Phys. Chem. C. 116 (2012) 8261–8270, http://dx.doi.org/10.1021/jp300806j.

[48] I. Edelman, O. Ivanova, R. Ivantsov, D. Velikanov, V. Zabluda, Y. Zubavichus, et al., Magnetic nanoparticles formed in glasses co-doped with iron and larger radius elements, J. Appl. Phys. 112 (2012) 084331, http://dx.doi.org/10.1063/1.4759244.

[49] I.S. Édelman, O.S. Ivanova, K.P. Polyakova, V.V. Polyakov, O.A. Bayukov, Evolution of the structure and magneto-optical properties of $Mn_xFe_{3-x}O_4$ films prepared by solid-state reactions, Phys. Solid State 50 (2008) 2289–2294, http://dx.doi.org/10.1134/S106378340812010X.

[50] K.J. Kim, H.S. Lee, M.H. Lee, S.H. Lee, Comparative magneto-optical investigation of d-d charge-transfer transitions in Fe_3O_4, $CoFe_2O_4$, and $NiFe_2O_4$, J. Appl. Phys. 91 (2002) 9974–9977, http://dx.doi.org/10.1063/1.1480482.

[51] C. Himcinschi, I. Vrejoiu, G. Salvan, M. Fronk, A. Talkenberger, D.R.T. Zahn, et al., Optical and magneto-optical study of nickel and cobalt ferrite epitaxial thin films and submicron structures, J. Appl. Phys. 113 (2013) 084101, http://dx.doi.org/10.1063/1.4792749.